THE ASTROPHYSICAL JOURNAL, 421:800–808, 1994 February 1

OBSERVING STELLAR CORONAE WITH THE GODDARD HIGH RESOLUTION SPECTROGRAPH. I. THE dMe STAR AU MICROSCOPII[1]

S. P. MARAN,[2] R. D. ROBINSON,[3] S. N. SHORE,[3,4] J. W. BROSIUS,[5] K. G. CARPENTER,[2] B. E. WOODGATE,[2]
J. L. LINSKY,[6] A. BROWN,[6] P. B. BYRNE,[7] M. R. KUNDU,[8] S. WHITE,[8] J. C. BRANDT,[9]
R. A. SHINE,[10] AND F. M. WALTER[11]

Received 1993 May 14; accepted 1993 August 5

ABSTRACT

We report on an observation of AU Mic taken with the Goddard High Resolution Spectrograph aboard the *Hubble Space Telescope*. The data consist of a rapid sequence of spectra covering the wavelength range 1345–1375 Å with a spectral resolution of 10,000. The observations were originally intended to search for spectral variations during flares. No flares were detected during the 3.5 hr of monitoring. A method of reducing the noise while combining the individual spectra in the time series is described which resulted in the elimination of half of the noise while rejecting only a small fraction of the stellar signal. The resultant spectrum was of sufficient quality to allow the detection of emission lines with an integrated flux of 10^{-15} ergs cm^{-2} s^{-1} or greater. Lines of C I, O I, O V, Cl I, and Fe XXI were detected. This is the first indisputable detection of the 1354 Å Fe XXI line, formed at $T \sim 10^7$ K, on a star other than the Sun. The line was well resolved and displayed no significant bulk motions or profile asymmetry. From the upper limit on the observed line width, we derive an upper limit of 38 km s^{-1} for the turbulent velocity in the 10^7 K plasma. An upper limit is derived for the flux of the 1349 Å Fe XII line, formed at $T \sim 1.3 \times 10^6$ K. These data are combined with contemporaneous GHRS and *IUE* data to derive the volume emission measure distribution of AU Mic over the temperature range 10^4–10^7 K. Models of coronal loops in hydrostatic equilibrium are consistent with the observed volume emission measures of the coronal lines. The fraction of the stellar surface covered by the footpoints of the loops depends upon the loop length and is less than 14% for lengths smaller than the stellar radius. From the upper limit to the estimated width of the Fe XXI line profile we find that we cannot rule out Alfvén wave dissipation as a possible contributor to the required quiescent loop heating rate.

Subject headings: methods: data analysis — stars: activity — stars: coronae — stars: individual (AU Microscopii) — stars: late-type — ultraviolet: stars

1. INTRODUCTION

AU Mic (HD 197481, Gleise 803) is a nearby (8.8 pc) dM0e star showing extreme levels of chromospheric and coronal activity. It has a phase-related photometric variation caused by starspots which has an amplitude in V of 0.12–0.35 mag (Torres & Ferraz Mello 1973) and a period of $4^d.865$. It is also known to undergo optical flaring activity, with a flare rate of 0.9 detectable flares per hour (Kunkel 1973) and has one of the largest ratios of time-integrated optical flare energy to bolometric energy of any of the flare stars in the solar neighborhood (Shakhovskaya 1989). It also has one of the largest fluxes of quiescent soft X-ray emission of any of the nearby flare stars, with measured fluxes of 2×10^{29} ergs s^{-1} (from *EXOSAT*) and 7×10^{29} ergs s^{-1} (from *Einstein*) (Pallavicini, Tagliferri, & Stella 1990).

The observations reported in this paper consist of a rapid time series of moderate-resolution UV spectra taken over the wavelength range 1345–1375 Å. This region contains spectral emission lines formed over a wide range of temperatures, including Fe XXI λ1354 (10×10^6 K), Fe XII λ1349 (1.3×10^6 K), O V λ1371 (2.5×10^5 K), C I λ1356 ($< 10^4$ K), and O I λ1355.6 ($< 10^4$ K). By examining the time history of these lines during the impulsive and decay phases of a stellar flare we planned to study the site of the original energy release as well as the characteristics of the energy-transfer and energy-loss processes.

Unfortunately, no flares were detected during the *HST* observing run. However, by combining the individual observations, it was possible to construct a good-quality spectrum which provides important information about the "quiescent" stellar atmosphere. In this paper we first describe the observations and data reduction, with special attention to the techniques used to reduce the background noise of the GHRS data. We then determine the fluxes and line profiles of the various emission lines and discuss their implications with regard to atmospheric properties.

[1] Based on observations with the NASA/ESA *Hubble Space Telescope*, obtained at the Space Telescope Science Institute, which is operated by the Association of Universities for Research in Astronomy, Inc., under NASA contract NAS5-26555.

[2] NASA/Goddard Space Flight Center, Laboratory for Astronomy and Solar Physics, Code 680, Greenbelt, MD 20771.
[3] Computer Sciences Corporation, NASA/Goddard Space Flight Center, Code 681, Greenbelt, MD 20771.
[4] Department of Interstellar Matter and Millimeter Astronomy, Observatoire de Paris, 5, Place Jules Janssen, F-92195 Meudon, France.
[5] Hughes STX Corporation, NASA/Goddard Space Flight Center, Code 682, Greenbelt, MD 20771.
[6] Joint Institute for Laboratory Astrophysics, University of Colorado, Campus Box 440, Boulder, CO 80309-0440.
[7] Armagh Observatory, College Hill, Armagh BT61 9DG, Northern Ireland, U.K.
[8] University of Maryland, Astronomy Department, College Park, MD 20742.
[9] University of Colorado, Laboratory for Atmospheric and Space Physics, Campus Box 392, Boulder, CO 80309-0392.
[10] Lockheed Research Laboratories, 3251 Hanover Street, Palo Alto, CA 94304.
[11] State University of New York, Stony Brook, Earth and Space Sciences Department, Stony Brook, NY 11794-2100.

2. OBSERVATIONS AND DATA REDUCTION

The active dMe star AU Mic was observed on 1991 September 4 with the Goddard High Resolution Spectrograph (GHRS) aboard the *Hubble Space Telescope*. The data consist of 30 minute spectral time sequences obtained during each of seven consecutive orbits. The rapid readout mode of operation was employed to ensure the maximum time resolution. In this mode the spectrograph takes a series of very short integration exposures, dumping each to the *HST* science tape recorder with a minimum of processing. We used 400 ms integrations to ensure that the data capacity of the tape recorders would not be exceeded. There is no increased noise induced by the large number of exposures.

The star was observed through the large science aperture (LSA) to ensure photometric accuracy. The observations were executed in coarse lock. A medium-resolution grating, G160M, was employed, resulting in a spectral coverage between 1345 and 1375 Å and a sampling of 0.06 Å per diode. A Pt wavelength calibration spectrum was taken before and after each sequence. This allowed us to determine the wavelength scale to an accuracy of ~ 5 km s^{-1}. It further enabled us to detect, and correct for, small shifts caused by thermal drifts in the spectrograph and the interaction of Earth's magnetic field with the detector. The largest drift observed over a single observing sequence was 0.2 diodes, or 3 km s^{-1}. In several cases a wavelength calibration exposure, normally taken in the ACCUM mode, was repeated in the rapid readout mode to check for possible errors induced by the mode of operation. The calibration spectra taken with the ACCUM and RAPID modes agreed with each other to better than 1 km s^{-1}.

To search for flares, the individual readouts were first integrated over the full wavelength range and then binned into time intervals ranging from 10 s to 5 minutes. The analysis was then repeated using only wavelength intervals containing known emission lines. This procedure showed that no detectable flares occurred during any of the seven orbits. This is confirmed by *IUE* observations and by ground-based photometry.

We next combined the individual readouts from all seven orbits to produce the highest quality spectrum possible. In doing this the major problem involved reducing the background noise. In quiescence, the spectral region chosen is extremely faint. Integrating over the entire 500 diodes in the array gave an average count rate of only 2.35 photons in an individual 0.4 s integration. This is very close to the dark count rate for the detector, caused principally by Cerenkov radiation from cosmic rays passing through the detector window (Rosenblatt et al. 1989). In Figure 1*a* we show the results of simply summing the entire set of observations. The expected spectral lines are evident, as is a pronounced "continuum" emission having an average of 145 counts per diode. Since this is a cool star we do not expect a real continuum at these wavelengths when it is in a quiescent state. We ascribe this apparent continuum to background noise. Removing the average background from the spectrum and integrating over the remaining emission lines shows that less than 2% of the observed counts (0.04 counts per readout) actually come from the star. With such count rates there is virtually no chance that more than one stellar photon would be detected during any individual 0.4 s integration period, so all counts in excess of 1 per readout are likely to be noise.

The basic scheme for noise reduction is therefore to reject all readouts having more than a specified number of counts before adding the readouts together. The actual rejection criterion involves a compromise between adding noise (for a large rejection factor) and losing signal (for low values). Since the noise dominates the star signal throughout the observations, we can use the data to obtain a reasonable estimate of the counting

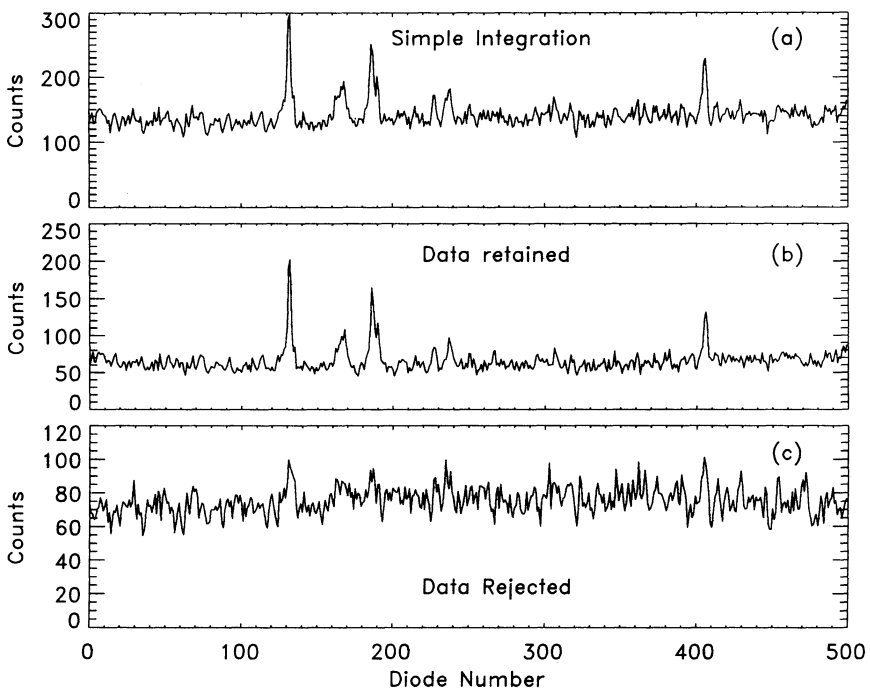

FIG. 1.—(*a*) Results of integrating individual spectra in the entire data set without regard to the level of noise. (*b*) Results of integrating individual spectra in which all samples with 5 or more counts have been rejected. (*c*) Integration of all samples which were rejected in producing the spectrum shown in (*b*).

TABLE 1

COUNTING STATISTICS FOR THE BACKGROUND NOISE

Counts (N)	$P(N)$	$P(\leq N)$
0.....	30.70	30.7
1.....	25.08	55.8
2.....	16.18	72.0
3.....	9.89	81.9
4.....	5.57	87.4
5.....	3.38	90.8
6.....	2.76	93.6
7.....	2.02	95.6
8.....	1.36	97.0
9.....	1.30	98.3
10.....	0.85	99.1

statistics for the background and then use these results to predict the amount of signal lost for any given rejection criterion. In Table 1 we present the counting statistics for the noise based upon an analysis of all 31,500 readouts in the data set. The minimum practical rejection criterion is to discard all readouts having 2 or more counts. In this case a stellar photon will be accepted into the integration only if the background count for that frame is 0, which, according to Table 1, happens $\sim$30% of the time. We thus reject 70% of the stellar photons. The background will have a single count 25% of the time, giving a total average background level of 16 counts per diode when integrated over the seven orbits. This is the minimum possible background which can be obtained from the data. In Table 2 we show the results of applying this analysis to other rejection criteria. Table 2 also shows the S/N values expected in stellar emission lines having an intrinsic count rate sufficient to produce 50, 200, and 500 counts in the integrated spectrum in the absence of background. These were calculated using the assumption of Poisson statistics, so that the total number of counts in the peak of the line, after background subtraction, is $S = NF_K R_L$, while the expected noise is $(\sigma^2) = NF_K(R_L + R_B)$. Here N is the total number of exposures (31,500 in this data set), F_K is the fraction of exposures which were not rejected during the analysis, R_L is the count rate per diode per exposure at the peak of the line, and R_B is the count rate in the background. The S/N value is then

$$\frac{S}{N} = \frac{NF_K R_L}{\sqrt{NF_K(R_L + R_B)}} = \sqrt{NR_L}\sqrt{\frac{F_K R_L}{R_L + R_B}}.$$

Note that the factor $(NR_L)^{1/2}$ is simply the expected S/N in the absence of background.

TABLE 2

EFFECTS OF NOISE REDUCTION

Rejection Criterion	Data Used (%)	Background (counts)	S/N (50)	S/N (200)	S/N (500)
2.....	31	16	4.24	9.90	16.26
3.....	56	36	4.24	10.75	18.11
4.....	72	50	4.17	11.16	18.84
5.....	80	67	4.03	11.20	19.23
6.....	85	78	3.95	11.18	19.43
7.....	89	89	3.95	11.17	19.59
8.....	92	100	3.89	11.06	19.63
9.....	94	107	3.82	11.03	19.63
10.....	95	113	3.78	11.00	19.64
$\leq$11.....	100	121	3.46	10.60	19.58

In Figure 1*b* we present the integrated spectrum after applying a rejection criterion of 5 counts, which we considered optimum for this data set. Figure 1*c* shows the integration of all rejected readouts, which account for $\sim$20% of the data. Note that the background level has been reduced by $\sim$50% and that there is very little stellar signal which has been rejected.

The final steps in the data reduction involved subtracting the average background from the integrated spectrum, dividing the spectrum by the total integration time, correcting for the dead diodes, and applying the absolute flux calibration. The flux calibration is a slowly varying function with a value at the central wavelength of the observation equal to 5.93×10^{11} counts s^{-1} diode^{-1} (ergs cm^{-2} s^{-1} Å^{-1})$^{-1}$. The calibrated spectrum is presented in Figure 2.

To supplement the GHRS observations we obtained a series of low-resolution *IUE* spectra with both the Long Wavelength Prime (LWP) and Short Wavelength Prime (SWP) cameras. To increase the number of time samples, each frame contained two exposures, taken with the star positioned near each end of the slit. A total of 10 SWP (23 minute) and 10 LWP (10 minute) exposures were obtained during the *IUE* shift containing the *HST* observations. The spectra were extracted from the processed line-by-line files using standard *IUE* software and a search was made for changes in the line and continuum flux. The SWP spectrum that was started $\sim$30 minutes before the start of *HST* observations showed an enhancement of the C IV (λ1550) line by a factor of 5 over the quiescent flux levels. However, the second exposure of the pair, taken $\sim$25 minutes later, showed only quiescent levels for all the lines. Subsequent SWP spectra also indicated no departure from quiescence, as do all of the LWP spectra.

To obtain the best possible data for the study of the quiescent atmosphere we added together the individual quiescent exposures using a weighted averaging technique similar to that described by Ayres et al. (1986). This technique eliminates the effects of particle hits and much of the fixed pattern noise as well as increasing the S/N of the spectrum. Fluxes from the individual emission lines were then extracted using a simple integration above the noise level for the SWP and an integration above an assumed absorption profile for the Mg II line in the LWP exposures. The results are presented in Table 3A.

3. RESULTS

Because of the point spread function of the *HST* optics resulting from the spherical aberration of the primary mirror,

TABLE 3A

FLUXES OF OBSERVED EMISSION LINES IN THE *IUE* SPECTRUM

Line ID	Laboratory Wavelength (Å)	Flux ($\times 10^{-14}$) (ergs cm^{-2} s^{-1})
O I	1304	8.4
C II	1335	13.9
Si IV/O IV	1397	6.9
C IV	1549	30.2
He II	1640	19.2
C I	1658	6.1
O III	1666	3.3
Si II/S I	1808	4.3
Si II/S I	1818	8.9
Mg II	2800	180

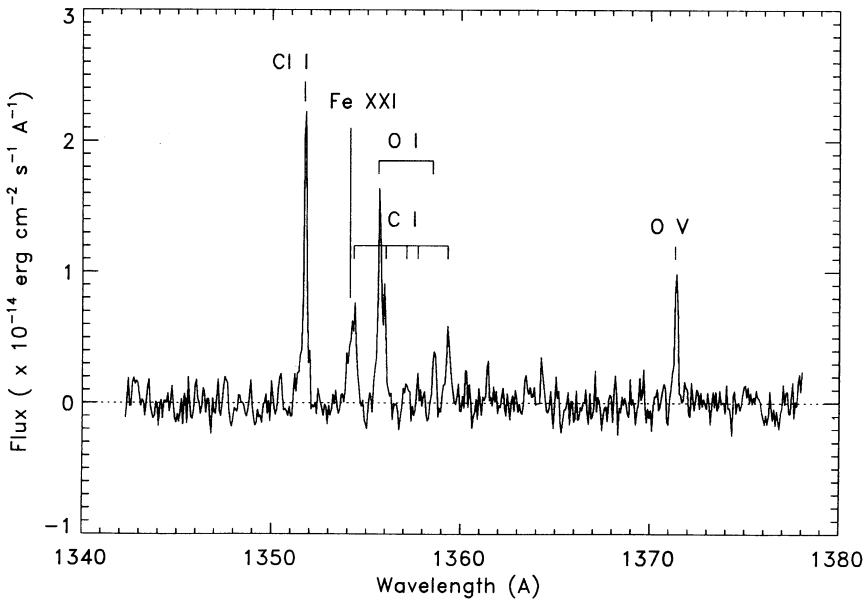

FIG. 2.—Final calibrated spectrum of AU Mic after background subtraction and noise reduction. A noise rejection criterion of 5 (as in the raw spectrum shown in Fig. 1*b*) was used in the analysis.

LSA spectra show distorted profiles. Inspection of the aperture map taken immediately after target acquisition also shows that the star was ~0".1 from the center of the aperture. This not only complicates the instrumental profile (see Fig. 3) but also introduces a small wavelength shift with respect to the calibration spectrum.

The observations are too noisy to attempt a spectral deconvolution, so we attempted a nonlinear least-squares fitting procedure to extract the quantitative data from the spectrum. We assumed that the intrinsic profile for all spectral lines was a Gaussian. We then specified an assumed strength, FWHM and central wavelength for the lines, generated a synthetic spectrum using these data, convolved the results with the modeled instrumental profile shown in Figure 3, and determined the rms deviation of the model profile from the observations. The parameters of the individual Gaussians were then iterated until the minimum deviation from the observations was obtained. The resultant fits for most of the emission lines are shown in Figure 4, while the calculated line parameters are given in Table 3B. Note the asymmetry in the individual lines caused by the decentering of the star in the aperture.

TABLE 3B

PROPERTIES OF OBSERVED EMISSION LINES IN GHRS SPECTRUM

Measured Wavelength (Å)	Line ID	Laboratory Wavelength (Å)	Flux ($\times 10^{-15}$) (ergs cm^{-2} s^{-1})	FWHM (Å)	RV
1351.70.....	Cl I	1351.657	5.6 ± 0.7	<0.11	9 ± 5
1354.11.....	Fe XXI	1354.14	2.4 ± 0.5	0.37	−7 ± 8
1354.32.....	C I	1354.29	1.1 ± 0.3	<0.1	6 ± 5
1355.62.....	O I	1355.598	3.6 ± 0.4	<0.1	6 ± 4
1355.89.....	C I	1355.844	1.9 ± 0.3	<0.1	9 ± 4
1357.15.....	C I	1357.134	0.4 ± 0.3	<0.1	3 ± 6
1357.70.....	C I	1357.659	0.5 ± 0.3	<0.1	7 ± 6
1358.55.....	O I	1358.512	1.1 ± 0.3	<0.1	8 ± 5
1359.30.....	C I	1359.275	1.5 ± 0.3	<0.1	5 ± 5
1371.32.....	O V	1371.292	2.4 ± 0.4	<0.1	6 ± 4
1218.36.....	O V[a]	1218.344	15.6 ± 0.9	<0.1	4 ± 5

[a] Data from observations reported by Woodgate et al. 1992.

Of special interest is the Fe XXI line at 1354.14 Å. This line is a forbidden transition within the ^3P ground state and is formed at temperatures near 10^7 K (Doschek et al. 1975; Cheng, Feldman, & Doschek 1979; Mason et al. 1979). This is the only line in the portion of the UV spectrum accessible to *HST* that samples this temperature regime. It always has negligible optical depth and hence is a good diagnostic of velocity fields. Unfortunately, it is also blended with a C I line at 1354.29 Å. To account for this blend in the analysis we used the moderately strong, isolated, C I line at 1359.28 Å to establish a width and radial velocity for the 1354.29 Å line. In fitting the blend we kept the position and width of the C I feature constant and allowed only its strength to vary. The Fe XXI line was allowed to vary in all three parameters. The results of the analysis are shown in Figure 5, which displays both the fit to the observations and the calculated intrinsic profiles for the two lines, i.e., how the spectrum would appear without the distortion produced by the broad instrumental profile. The line parameters are shown in Table 3B.

Note that the Fe XXI line is well represented by a single Gaussian with no pronounced asymmetry in either the red or blue wings. The central wavelength shows no sign of large radial velocity in the stellar rest frame and the width of the line is fully consistent with a thermal Doppler velocity distribution from a plasma with temperature near 10^7 K. The form of the line is similar to that seen in the Sun during solar flares (e.g., Cheng, Feldman, & Doschek 1979).

In Figure 6 we show the spectral region containing the Fe XII 1349.37 Å line, formed at ~1.3×10^6 K. There is no obvious spectral feature at this location, so we can only derive an upper limit to the Fe XII flux. Most of the flux from this line should appear in 3 pixels. From the characteristics of the background-subtracted spectrum we know that the non-emission-line regions have a mean of zero and a variance of 7 counts per diode. From this we know that the distribution of counts within a sum of 3 pixels is a normal distribution with mean of

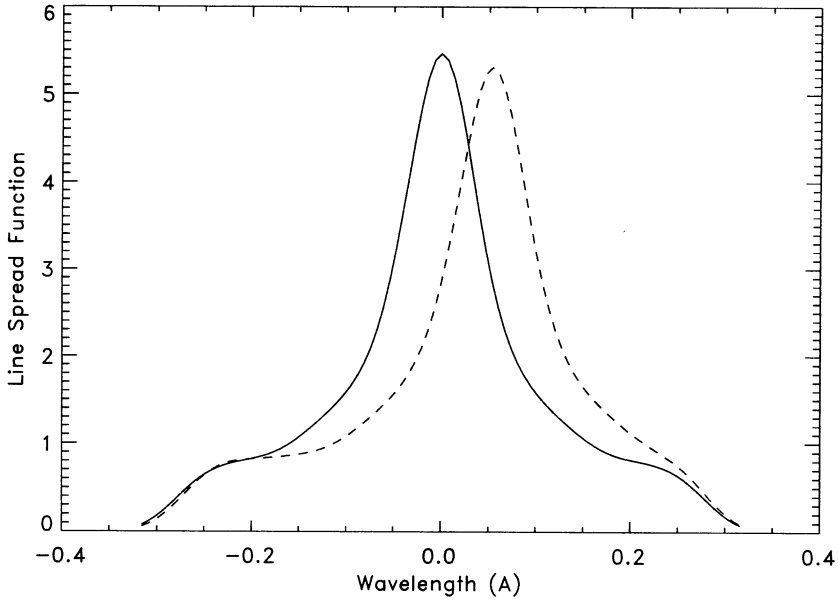

FIG. 3.—Calculated line spread function (LSF) for the G160M grating used with the 2″ aperture. The solid line shows the LSF for a source which is centered in the aperture, while the dashed line is the LSF when the source is shifted 0.″1 from the center of the aperture.

zero and a variance of 11. A 3 σ detection, therefore, requires 33 counts, or a flux of 1.0×10^{-15} ergs cm^{-2} s^{-1}, which is taken as the upper limit to the Fe XII flux.

4. EMISSION MEASURE DISTRIBUTION

The volume emission measure (VEM) distribution of AU Mic between 10^4 and 10^7 K was calculated by combining the GHRS data with contemporaneous *IUE* data. The general method and atomic data used are those of Brown et al. (1984). The calculation for Fe XXI used the collision strengths and excitation rates of Aggarwal (1991) and the *A*-values listed by Mason et al. (1979). For Fe XII the collision strengths of Tayal, Henry, & Pradhan (1987) and the level populations of Tayal et al. (1991) were used. Level populations were computed as a function of electron density to satisfy these atomic data.

The resulting VEM distribution is shown in Figure 7. The

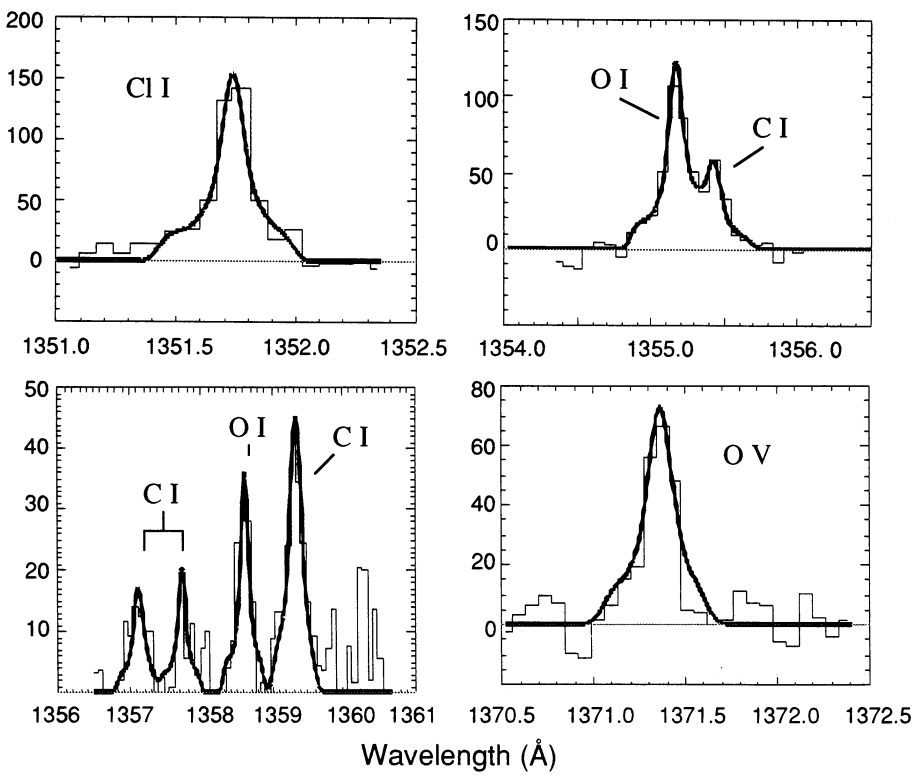

FIG. 4.—Observed profiles of various emission lines (*histograms*) overplotted with the line fits (*heavy solid lines*). The fits assume an intrinsic Gaussian profile convolved with a decentered line spread function (see Fig. 3).

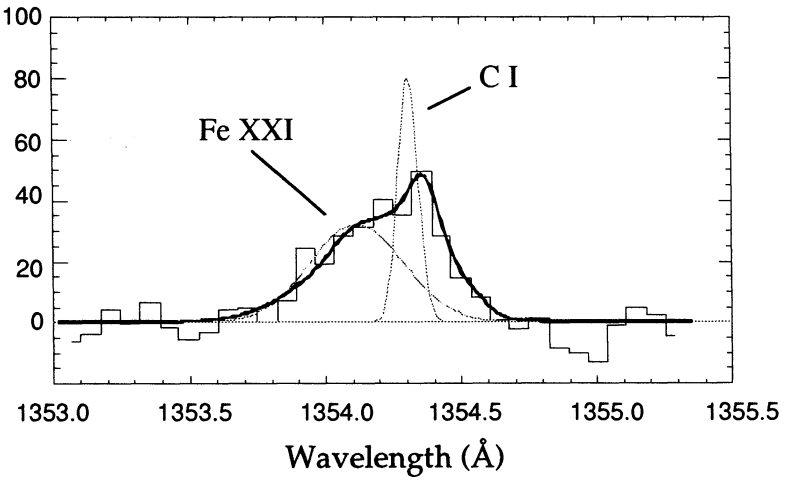

FIG. 5.—Comparison of the observations (*histogram*) with the computed line fit (*heavy solid line*) in the Fe XXI region. The assumptions described in Fig. 4 apply. The C I line is fixed in position and width while the Fe XXI line is allowed to vary in strength, position, and width during the fitting process. Also shown (*dotted lines*) are the calculated line profiles for the Fe XXI and C I lines after removal of the instrumental smearing. The small wavelength offset between the observations and the calculated line profiles results from a decentering of the star in the aperture.

emission measure loci for Fe XXI are entirely consistent with the VEM derived from the *EXOSAT* Lexan count rate given by Pallavicini et al. (1990) as calculated using the method of Brown et al. (1991). It should be remembered that while the flux seen in the Fe XXI line comes from a restricted range of temperature, the flux contributing to the broad-band *EXOSAT* measurement originates from a much wider temperature range resulting in a higher count rate than from 10^7 K plasma alone. The Fe XII upper limit restricts the allowed VEM at 1.3×10^6 K to be barely larger than at 2.5×10^5 K, where the O V lines are formed.

By combining our observation of the O V 1371 Å flux with the O V 1218 Å flux measured from data taken by Woodgate et al. (1992), we were able to make a direct measurement of the transition region electron density. The line ratio calibrations of Dufton et al. (1978) for an electron temperature of 2.5×10^5 K and the observed ratio of O V 1371/O V 1218 $\sim$0.153 imply an electron density of 5×10^{10} cm^{-3}. The emission measure loci for the O III 1666 Å line provide an electron density which is consistent with this value.

5. DISCUSSION

In Figure 8 we show *Skylab* spectra of a solar flare and a solar active region taken over a wavelength range similar to that of the *HST* observations (Cohen 1981). Comparing these with Figure 2 shows the striking similarity of the AU Mic spectrum to that of a solar flare. Although the *IUE* satellite did show the presence of enhanced UV emission less than 30 minutes prior to the onset of the *HST* observations, there is no evidence for detectable flare activity during the *HST* observations from either the *HST* data themselves or from concurrent ground-based optical photometry or the *IUE*. We therefore conclude that the integrated GHRS spectrum represents a steady state condition on the star.

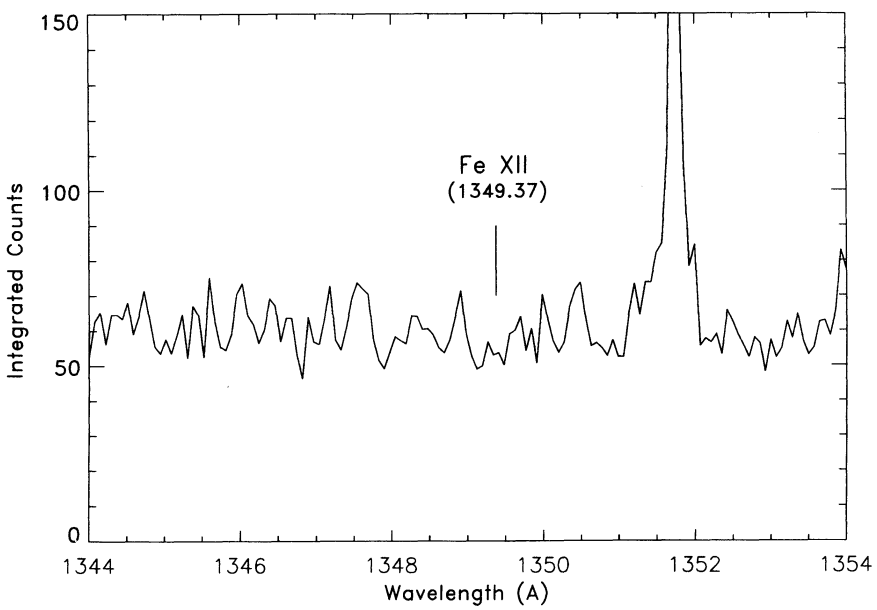

FIG. 6.—An expanded view of the observations showing the region where Fe XII is expected

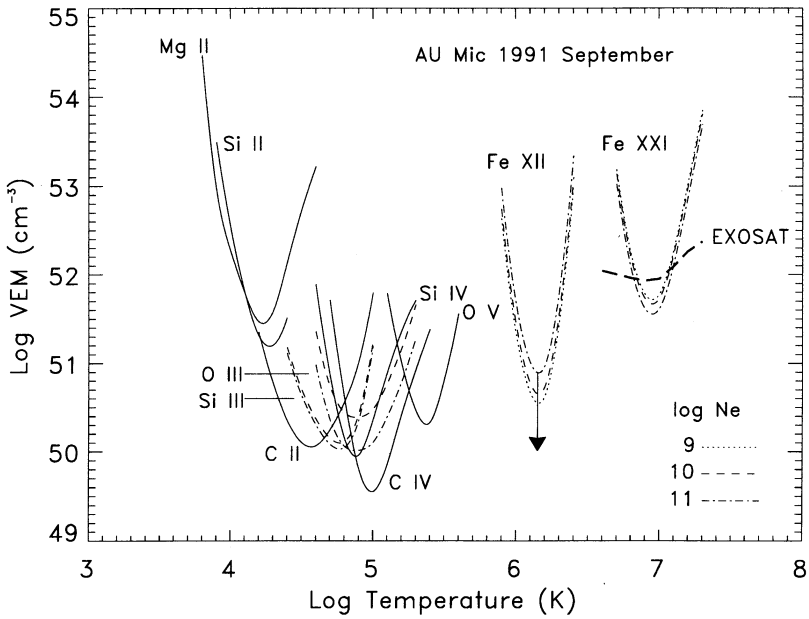

FIG. 7.—Volume emission measure over the temperature range 10^4–10^7 K using simultaneous GHRS and *IUE* spectra

5.1. Fe XXI *Line Width*

Fe XXI 1354 Å is the broadest line in our GHRS spectrum (see Table 3B). Its width of 0.37 Å (instrumental profile removed) is somewhat less than that observed during solar flares, but, as in the case of solar flares, its central wavelength shows no Doppler shift indicative of large radial bulk motions (Cheng, Feldman, & Doschek 1979). Lower and upper limits on the calculated line width—0.30 and 0.50 Å—enable us to place constraints on both the temperature and the nonthermal random mass motions in the Fe XXI emitting region. Assuming first that the line width is due entirely to thermal Doppler broadening, we obtain log $T = 6.73$, 6.91, and 7.17, respectively, for the lower limit, best fit, and upper limit values. Comparing the Fe XXI abundance fractions at these three temperatures using the ionization equilibrium calculations of Arnaud & Raymond (1992), we find it unlikely that plasma at the lower temperature is responsible for the Fe XXI emission, since the ion fraction at this temperature is two orders of magnitude less than that at its peak value (which occurs at log $T = 7.0$). However, at the higher temperature values the Fe XXI fraction is down by factors of only 2 and 4, respectively, from its peak value. In light of the uncertainties, we will assume for simplicity in subsequent calculations that the Fe XXI emission forms at its temperature of peak ionization fraction.

When two or more line broadening mechanisms produce Gaussian profiles, then the line widths due to the individual broadening mechanisms add quadratically to produce the total width. Using the maximum value of 0.5 Å for the Fe XXI line width, along with a plasma temperature of 10^7 K, we obtain an upper limit on the most probable velocity of 38 km s^{-1} that will be used later when we discuss the plausibility of coronal heating via Alfvén wave dissipation.

5.2. *Coronal Loop Models*

AU Mic has previously been observed with both the *Einstein Observatory* and *EXOSAT*. *Einstein* Imaging Proportional Counter (IPC) pulse height spectra can be well fitted with two isothermal components at different temperatures (Schmitt et al. 1987), while *EXOSAT* Channel Multiplier Array (CMA) observations yield only a high-temperature component (Pallavicini et al. 1988). Despite the fact that the two instru-

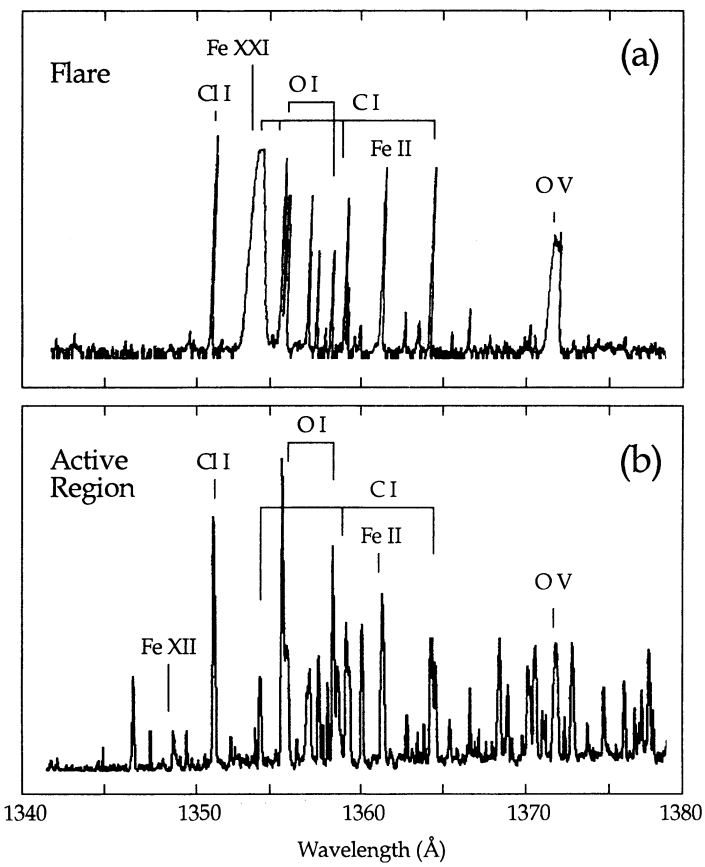

FIG. 8.—*Skylab* observations (from Cohen 1981) showing sample spectra of a moderate sized solar flare (*a*) and a strong solar plage (*b*).

ments disagree quantitatively the observations do indicate that high-temperature ($\sim 10^7$ K) plasma exists on flare stars in general even during quiescence. Although many stellar X-ray observations have been analyzed using a two-temperature fit, it is well known that solar X-ray loops are far from isothermal. A better approach to the stellar problem is therefore, to calculate X-ray spectra using loop models that incorporate a continuous temperature distribution. Stern, Antiochos, & Harnden (1986), using the code developed by Vesecky, Antiochos, & Underwood (1979) to calculate hydrostatic loop models, concluded that active F–G dwarf X-ray emission is dominated by an ensemble of loops with a maximum temperature ~ 10–15×10^6 K, a high pressure ($\gtrsim 400$ dynes cm^{-2}), a short length ($< 10^{10}$ cm), and a small variation of cross section from the base to the top of the loops. In the limit of low gravity and constant cross section the numerical code used by Stern, Antichos, & Harnden (1986) yields results equivalent to the analytical expressions derived by Rosner, Tucker, & Vaiana (1978, hereafter RTV). We therefore employ the formulae derived by the latter authors to analyze the AU Mic spectrum.

The RTV formulae were derived assuming cylindrical loops with no bulk motions and no net mass fluxes. The pressure is taken to be constant along the loops. Temperature and density are determined by the energy balance relation, and the local mechanical heating function is assumed to be constant throughout the loop. The radiative loss function has been approximated by an analytic expression which ultimately depends upon numerous atomic parameters as well as solar elemental abundances[12].

[12] It should be pointed out that our observed VEM calculations, as well as the plasma parameters obtained using *Einstein* and *EXOSAT*, also depend upon the assumption of solar photospheric element abundances. Meyer (1993) has shown, however, that although elements with a high first ionization potential (FIP) have the same abundance (relative to hydrogen) in the solar corona as in the solar photosphere, elements with a low FIP (such as Fe) are frequently enhanced by factors of ~ 4.5 relative to their respective photospheric abundances. We have not attempted to compensate for the FIP bias processes in our analysis.

In the RTV picture, the coronal loops can be fully characterized by specifying their length L_T and a maximum apex temperature T_{max}. From these it is possible to specify a pressure and heating rate, a temperature distribution, and a consequent density distribution using the RTV expressions. Knowing the temperature variation along the loop, we can then calculate the lengths of the loop within which the Fe XXI emission ($6.9 \leq \log T \leq 7.1$) and the Fe XII emission ($6.0 \leq \log T \leq 6.2$) originate. We find that although the density of the low-temperature plasma is nearly an order of magnitude greater than that of the high-temperature plasma, the length of the portion of the loop containing the high-temperature plasma is nearly three orders of magnitude greater than that of the low-temperature plasma. Thus, for a constant loop cross section, the volume emission measure of the 10^7 K plasma is a factor of ~ 10 greater than that of the 10^6 K plasma. Using the measured VEM of the 10^7 K plasma along with the length of the loop containing the hot plasma and the electron densities which were determined from the loop model also allows us to calculate the total cross sectional area of the emitting volume and, therefore, the expected area coverage of the loop footpoints on the stellar surface.

In Tables 4 and 5 we present the results of calculations covering a range of loop parameters. All of the loops listed are hydrostatically stable, as they are all shorter then twice their respective pressure scale heights (Serio et al. 1981). In all of the cases considered the ratio of emission measures between the 10^7 and 10^6 K plasmas is consistent with the observations, indicating that as long as the maximum loop temperature is near 10^7 K, that temperature will dominate. For much higher maximum temperatures the length of the loop over which the plasma at 10^7 K exists decreases and the emission measure ratio drops.

Surprisingly, the VEM ratio is independent of loop length. However, the expected fractional coverage of the star increases with increasing loop length, caused mainly by the lower densities in the longer loops. We note that Saar (1994) has recently

TABLE 4

VARIATION OF LOOP PROPERTIES WITH LOOP LENGTH FOR T_{max} = constant = 1.5×10^7 K

L_T/R_*	p	log N_e(7.0)	log N_e(6.1)	E_H	VEM(7)/VEM(6.1)	Coverage	B_A
0.1.....	560	11.3	12.2	2.6	11.2	0.014	>8600
0.3.....	190	10.8	11.7	0.29	11.2	0.042	>5000
0.5.....	110	10.6	11.5	0.10	11.2	0.071	>3900
1.0.....	56	10.3	11.2	0.026	11.2	0.14	>2700
2.0.....	28	10.0	10.9	0.0064	11.2	0.28	>1900

NOTES.—L_T/R_* is the total loop length as a fraction of the stellar radius, p is the loop pressure in dyne cm^{-2}, N_e(7.0) and N_e(6.1) are the electron density in cm^{-3} at log T = 7.0 and log T = 6.1, respectively, E_H is the loop heating rate in ergs cm^{-3} s^{-1}, VEM(7)/VEM(6.1) is the ratio of the volume emission measures of the 10^7 and the $10^{6.1}$ K plasmas, Coverage is the fraction of the stellar surface area covered by loop footpoints, and B_A is the lower limit on the magnetic field (in Gauss) required for Alfvén wave dissipation to yield the loop heating rate.

TABLE 5

VARIATION OF LOOP PROPERTIES WITH T_{max} FOR LOOP LENGTH = constant = $0.5R_*$

T_{max}	p	log N_e(7.0)	log N_e(6.1)	E_H	VEM(7)/VEM(6.1)	Coverage	B_A
1.0.....	33	10.1	11.0	0.025	26.6	0.10	>1700
1.3.....	73	10.4	11.3	0.062	14.6	0.083	>2900
1.5.....	110	10.6	11.5	0.10	11.2	0.071	>3900
2.0.....	260	11.0	11.9	0.28	9.28	0.036	>6900
3.0.....	890	11.5	12.4	1.2	8.46	0.012	>15000

NOTES.—T_{max} is the loop maximum temperature in units of 10^7 K; all other parameters are the same as in Table 4.

measured the strength and area coverage of magnetic fields on AU Mic and concludes that they cover up to 55% of the surface with an average strength of ~4200 G. If these fields are the same as those containing the hot coronal plasma, then the loops should be large, perhaps exceeding 2 stellar radii, R_*, in total length. These long loops have the advantage of requiring a much smaller heating rate to maintain their large temperatures. On the other hand, if the measured fields are in the form of low lying loops (with lengths of $0.5R_*$ or less) then only a very small fraction can contain the hot plasma and the remainder must have temperatures smaller than 10^6 K, so that they do not generate a significant amount of Fe XII flux.

Finally, we have used our model to calculate the density of the plasma emitting the O V (2.5×10^5 K) radiation. Values in excess of 10^{12} cm^{-3} were calculated, which is more than an order of magnitude greater than those deduced from the O V λ1371 to λ1218 ratio. Also, the volume emission measure for O V predicted from the model is considerably smaller than the observed value. These are either manifestations of the crudeness of the model, or indications that the bulk of the observed O V emission originates in structures other than the loops that contain the 10^7 K plasma. In other words, the apparent discrepancy between our model calculations and the O V observations suggests that the majority of the O V emission originates in separate, cooler, less dense loops.

5.3. *Coronal Heating*

The (constant) heating rate E_H for each model loop can be calculated from the RTV loop parameters and is listed in Tables 4 and 5. This can be multiplied by the total loop volume to obtain the total power required by the emitting volume. Consider Alfvén wave dissipation as a possible mechanism for supplying this heating in the quiescent loop models. The Alfvén wave energy flux can be written $F_A = \frac{1}{2}\rho(\delta v_A)^2 V_A$ ergs cm^{-2} s^{-1} (e.g., Jacques 1977), where ρ is the mass density, δv_A is the wave amplitude, and V_A is the Alfvén speed [$V_A = B(4\pi\rho)^{-1/2}$]. Using the electron density obtained for the 10^7 K plasma, and using the upper limit on the most probable nonthermal velocity (obtained from the upper limit on the Fe XXI line width) for the wave amplitude, we obtain a lower limit on the magnetic field strength, B_A, such that the Alfvén wave energy flux passing through the cross section area of the loop balances the total power required by the loop. This assumes that all of the Alfvén wave energy can actually be dissipated within the loop. The lower limits on the magnetic field strength are listed in Tables 4 and 5. The plasma β parameter corresponding to these field strengths is $\beta = (8\pi p/B_A^2) \sim 10^{-4}$, comparable to the values obtained from parameters given by Brosius et al. (1992) for a quiescent solar coronal active region loop. Thus, although we cannot present a strong case for Alfvén wave heating of the hot model loops, neither can we definitely rule it out.

6. CONCLUSIONS

We report the results of an observing run on the active dMe star AU Mic using the GHRS aboard the *Hubble Space Telescope*. The observations were taken in rapid readout mode and it was found that by judiciously rejecting spectral samples with large noise content it was possible to reduce the overall noise background in the integrated observations by a factor of 2. This is significant since the stellar signal had a count rate less than 2% of the background. We suggest that this observing mode is worth using for any weak source in which background subtraction is important.

In a total of 3.5 hr of integration we were able to obtain a spectrum in which emission lines with integrated fluxes greater than 1.0×10^{-15} ergs cm^{-2} s^{-1} could be reliably detected. This spectrum, which represents the "quiescent" state of the star, strongly resembles the spectrum of a solar flare.

This is the first time that the Fe XXI 1354.1 Å line, formed at temperatures ~10^7 K, has been resolved on a star other than the Sun. The profile shows no centroid shift indicative of a large bulk velocity, in agreement with observations of the line during moderate-sized solar flares. The width of the line is consistent with a thermal Doppler velocity distribution in a 10^7 K plasma. From the upper limit on the observed line width we obtain an upper limit of 38 km s^{-1} for the nonthermal velocity. The Fe XII 1349.4 Å line, formed at 1.3×10^6 K, is not detected.

Using simple hydrostatic loop models we can account for the relative VEM ratio between the Fe XXI and Fe XII emitting plasma. We also examine the expected surface area coverage for the loops and present arguments in favor of the loops having lengths of 2 or more stellar radii.

Using an Alfvén wave amplitude equal to the upper limit of the nonthermal velocity, we calculate the lower limit on the magnetic field such that Alfvén wave dissipation balances the loop heating rate. Field strengths in excess of several thousand Gauss are required.

We thank the staff of the Space Telescope Science Institute for their outstanding effort in scheduling these observations even in the face of uncertain instrument performance. We thank the referee, M. Giampapa, for helpful suggestions. Support for this work was provided by NASA through Guaranteed Time Observer funding to the GHRS science team and grant NAGW-2904 to the University of Colorado.

REFERENCES

Aggarwal, K. M. 1991, ApJS, 77, 677
Arnaud, M., & Raymond, J. 1992, ApJ, 398, 394
Ayres, T. R., Judge, P. G., Jordan, C., Brown, A., & Linsky, J. L. 1986, ApJ, 311, 947
Brosius, J. W., Willson, R. F., Holman, G. D., & Schmelz, J. T. 1992, ApJ, 386, 347
Brown, A., Drake, S. A., Van Steenberg, M. E., & Linsky, J. L. 1991, ApJ, 373, 614
Brown, A., Jordan, C., Stencel, R. E., Linsky, J. L., & Ayres, T. R. 1984, ApJ, 283, 731
Cheng, C.-C., Feldman, U., & Doschek, G. A. 1979, ApJ, 233, 736
Cohen, L. 1981, NASA RP, 1069
Doschek, G. A., Feldman, U., Dere, K. P., Sandlin, G. D., Van Hoosier, M. E., Brueckner, G. E., Purcell, J. D., & Tousey, R. 1975, ApJ, 196, L83
Dufton, P. L., Berrington, K. A., Burke, P. G., & Kingston, A. E. 1978, A&A, 62, 111
Jacques, S. A. 1977, ApJ, 215, 942
Kato, T., Lang, J., & Berrington, K. E. 1990, Atomic Data Nucl. Data, 44, 133
Kunkel, W. E. 1973, ApJS, 25, 1
Mason, H. E., Doschek, G. A., Feldman, U., & Bhatia, A. K. 1979, A&A, 73, 74
Meyer, J.-P. 1993, Adv. Space Res., 13, No. 9, 377
Pallavicini, R., Monsignori-Fossi, B. C., Landini, M., & Schmitt, J. H. M. M. 1988, A&A, 191, 109
Pallavicini, R., Tagliferri, G., & Stella, L. 1990, A&A, 228, 403
Rosenblatt, E. I., Beaver, E. A., Cohen, R. D., Linsky, J. B., & Lyons, R. W. 1989, in Electron Image Tubes and Image Intensifiers II (Proc. SPIE, 1499), 72
Rosner, R., Tucker, W. H., & Vaiana, G. S. 1978, ApJ, 220, 643 (RTV)
Saar, S. H. 1994, ApJ, in press
Schmitt, J. H. M. M., Pallavicini, R., Monsignori-Fossi, B. C., & Harden, F. R., Jr. 1987, A&A, 179, 193
Serio, S., Peres, G., Vaiana, G. S., Golub, L., & Rosner, R. 1981, ApJ, 243, 288
Shakhovskaya, N. I. 1989, Sol. Phys., 121, 375
Stern, R. A., Antiochos, S. K., & Harnden, F. R., Jr. 1986, ApJ, 305, 417
Tayal, S. S., Henry, R. J. W., Keenan, F. P., McCann, S. M., & Widing, K. G. 1991, ApJ, 369, 567
Tayal, S. S., Henry, R. J. W., & Pradhan, A. K. 1987, ApJ, 319, 951
Torres, C. A. O., & Ferraz Mello, S. 1973, A&A, 27, 231
Vesecky, J. F., Antiochos, S. K., & Underwood, J. H. 1979, ApJ, 233, 987
Woodgate, B. E., Robinson, R. D., Carpenter, K. G., Maran, S. P., & Shore, S. N. 1992, ApJ, 397, L95